

Nonlinear Evolutionary PDE-Based Refinement of Optical Flow

Hirak Doshi, N. Uday Kiran

Abstract

The goal of this paper is propose a mathematical framework for optical flow refinement with non-quadratic regularization using variational techniques. We demonstrate how the model can be suitably adapted for both rigid and fluid motion estimation. We study the problem as an abstract IVP using an evolutionary PDE approach. We show that for a particular choice of constraint our model approximates the continuity model with non-quadratic regularization using augmented Lagrangian techniques. We subsequently show the results of our algorithm on different datasets.

Keywords. Optical Flow, Fluid Flow, Rigid Motion, Variational Methods, Evolutionary PDE, Augmented Lagrangian.

Mathematics Subject Classification 2020. 35A15, 35J47, 35Q68.

1 Introduction

Optical flow plays a key role in many advanced Computer Vision applications. It is a rich source of information of perceptible motion in our visual world. It's reliable estimation is thus important and at the same time, challenging. Assuming the principle of local conservation of intensity and small temporal variations, optical flow involves recovery of a function $\mathbf{u} = (u, v)$ such that

$$f(\mathbf{x}, \tau) = f(\mathbf{x} + \mathbf{u}, \tau + \Delta\tau).$$

where $f : \Omega \times [0, T] \rightarrow \mathbb{R}$ if the image sequence and $\Omega \subset \mathbb{R}^2$ is open and bounded. This establishes a correspondence between pixel motions. Using first order approximations the above relation can be written as

$$f_\tau + \nabla f \cdot \mathbf{u} = 0, \tag{1}$$

which is widely known as the Optical Flow Constraint (OFC). Recasting the constraint as a variational minimization we can write (1) as

$$\min_{\mathbf{u}} J_1(\mathbf{u}) = \int_{\Omega} (f_t + \nabla f \cdot \mathbf{u})^2.$$

This is the simplest least-square minimization. This problem is ill-posed as it leads to the aperture problem. Additional regularization terms are necessary to ensure well-posedness. The most common regularization term is the quadratic smoothness penalizing the gradient of the components of the flow originally introduced by Horn and Schunck [21] in their seminal work. Early improvements to this model was suggested by Nagel [29] and subsequently by others. Cohen [9] and Kumar et.al. [22] used the L^1 regularization which is more robust to outliers and preserves important edge informations. A new discontinuity preserving optical flow model with L^1 norm on the OFC was proposed by Aubert et. al. [3]. They imposed an additional weighted term to account for the homogeneous regions. They studied the problem in the space of functions of bounded variations $BV(\Omega) \times BV(\Omega)$. The well-posedness of the HS model as well as Nagel model was studied by Schnörr [35] in the space $H^1(\Omega) \times H^1(\Omega)$. Taking a step further, the authors in [8] proposed a $L^p - TV/L^p$ ($p = 1$ or 2) model combining both L^1 and L^2 terms. The behaviour of their regularization term is similar to the Huber function:

$$H(x; \epsilon) = \begin{cases} \frac{x^2}{2\epsilon}, & 0 \leq |x| \leq \epsilon \\ |x| - \frac{\epsilon}{2}, & |x| > \epsilon. \end{cases}$$

A detailed review and rigorous analysis of several variational optical flow models within the framework of calculus of variations can be found in [20].

Though most of the estimation involving rigid or quasi-rigid motion can be handled by OFC, it is insufficient to provide an accurate estimation for fluid-based images. Traditional computer vision techniques may not be suitable to capture these deformations of brightness patterns because of the high spatio-temporal turbulence in these sequences. These reasons have motivated researchers to look for an alternate constraint which can not only preserve pixel-correspondence but also capture certain intrinsic features of the flow. This paradigm shift hints at constraints which are physics-dependent. Schunck [33, 34] initially proposed the idea of Extended Optical Flow Constraint (EOFC). He observed the similarities between EOFC and conservation of mass in fluid dynamics and suggested to use this as a motion constraint equation. In [5] the authors describe a Generalized Optical Flow Constraint (GOFC) and give it's physical interpretation. They further

propose a unifying model linking both GOF and EOF. Moving away from the standard a-priori smoothness terms Corpetti [11, 13] proposed the use of divergence-curl regularization penalizing the divergence and the curl of the flow. It was observed that first order divergence-curl regularization cannot preserve fine structures in turbulent flows. To overcome this problem the authors in [12] proposed the use of a second-order divergence-curl regularization that preserves spatial characteristics and vortices of the flow. Luttmann et. al. [26] suggested a method where the flow can be computed directly as a potential (respectively stream) flow. This is possible by the assumption that locally, the flow field can be expressed as the gradient of a potential (respectively stream) function. This is computationally efficient as it requires solving one minimization problem rather than two. A detailed review and synopsis of fluid motion estimation methods using variational techniques can be found in [19]. Here the authors give a clear physical interpretation of the continuity equation based constraint:

$$f_\tau + \nabla f \cdot \mathbf{u} + f \nabla \cdot \mathbf{u} = 0; \quad (2)$$

The additional term $f \nabla \cdot \mathbf{u}$ is the non-conservation of the brightness function due to loss of particles caused by non-null out of plane component. If incompressibility conditions are imposed then the OFC can be viewed as a divergence-free approximation of the CEC. It is thus natural to use the non-conservation term as an additional constraint to extract flow informations.

In this context, we have proposed a constraint-based refinement of optical flow [16]. The idea behind such a refinement principle is to have a general framework for fluid motion estimation such that

1. pixel correspondence is retained
2. spatial characteristics and vortices are preserved.

As a concrete example we considered the HS optical flow (u_0, v_0) as an initial estimate. Further using an image-driven evolutionary PDE model resulting from a quadratic regularization we have shown the well-posedness of such a refinement principle. An important characteristic of the model is the possibility of a diagonalization by the Cauchy-Riemann operator leading to a decoupled system involving diffusion of the curl and a multiplicative perturbation of the laplacian of the divergence of the flow. For a specific case it was derived that the model is actually close to physics-based model [24] using a modified augmented Lagrangian method.

The current work aims to extend this work using a non-quadratic L^1 regularization approach. Starting with an initial estimate we obtain this refinement using the following evolutionary PDE:

$$\begin{cases} \frac{\partial u}{\partial t} = \Delta_1 u + a_0 \frac{\partial}{\partial x} [\phi(f)(u_x + v_y)] \\ \frac{\partial v}{\partial t} = \Delta_1 v + a_0 \frac{\partial}{\partial y} [\phi(f)(u_x + v_y)], \end{cases} \quad (3)$$

where Δ_1 is the 1-laplacian operator which has been widely studied in many image-processing applications, see for example [2, 18, 27, 28]. The main advantage of this model is that it can be potentially adapted to rigid, quasi-rigid and fluid motion estimation. As before for a specific case we show the closeness of our model with the continuity equation model with L^1 regularization using the augmented Lagrangian framework.

Unlike OFC which measures pixel displacements, the physics-based constraint measure pixel velocities. The velocity field is the projected motion of a real 3D object velocity on the image plane [15]. If ρ denotes the object density assuming that the incident light is parallel to z -axis, the projection of intensity can be measured by the relation

$$f(x, y, \tau) = \int_{z_1}^{z_2} \rho(x, y, z, \tau) dz.$$

This approach was taken by Wildes et. al. [39] where they derived the relation between the physics-based continuity equation and its equivalent image-intensity version. Further using fluid mechanics principle Liu and Shen [25] established a link between fluid flow and optical flow estimation. Here optical flow is assumed to be proportional to the path-averaged velocity of fluid within a relevant field quantity. A detailed mathematical analysis of physics-based optical flow model in $BV(\Omega) \times BV(\Omega)$ was done by Wang et.al. [36]. The mathematical setting for our problem is $[W^{1,p}(\Omega) \cap L^2(\Omega)]^2$ in the limiting case $p \rightarrow 1$. The augmented Lagrangian framework further allows us to establish a link between our model and the continuity equation model. We also believe that this framework can be adopted to a deep learning paradigm.

The rest of the paper is organized as follows. In Section (2.1) give a description of our refinement model. Subsequently in Section (2.2) we discuss the general well-posedness results and study the system using an evolutionary PDE set up. Next in Section (2.3) we show that how for a particular choice of constraint the refinement model closely approximates the continuity equation with L^1 regularization. Finally in Section (3) we perform several numerical experiments and show our results on different datasets.

2 Abstract Framework

2.1 Mathematical Formulation

As mentioned above, our main goal is to propose a general framework for optical flow given an initial flow field. We choose the HS optical flow as our initial estimate as it is a reasonably good starting solution because of its assured well-posedness. The model we propose is the following:

$$J_{1,R}(\mathbf{u}) = \beta \int_{\Omega} \phi(f) \psi(\nabla \mathbf{u}) + \alpha \int_{\Omega} \{|\nabla u| + |\nabla v|\} \quad (4)$$

where ψ depends on the components of the flow and its derivatives and ϕ corresponds to an image-dependent weight term which makes the refinement process image-driven. If $\phi(f) \equiv 1$ then the refinement process is completely flow-driven. The constants α, β are weight parameters. We assume that both the functions ϕ and ψ are real-valued smooth functions. Moreover, we assume ϕ a monotone increasing function. Different choices for ϕ and ψ can be made depending on the geometric features. In this particular work we choose ψ as the one which penalizes the divergence of the flow, i.e. $\psi = (\nabla \cdot \mathbf{u})^2$. In this case the refinement functional becomes

$$J_{1,R}(\mathbf{u}) = \beta \int_{\Omega} \phi(f) (\nabla \cdot \mathbf{u})^2 + \alpha \int_{\Omega} \{|\nabla u| + |\nabla v|\}. \quad (5)$$

It is well-known that the functional is coercive in $BV(\Omega) \cap L^2(\Omega)$, see [27]. Also the functional is convex but not strictly convex because of the total variation term. Hence uniqueness is not assured. However using Theorem 5, section 8.2.4 in [17] the existence of minimizer is guaranteed.

2.2 Mathematical Analysis

In this section we discuss the problem using an evolutionary PDE approach. This will be studied by considering the following approximation

$$J_{p,R}(\mathbf{u}) = \beta \int_{\Omega} \phi(f) (\nabla \cdot \mathbf{u})^2 + \frac{\alpha}{p} \int_{\Omega} \{|\nabla u|^p + |\nabla v|^p\}, \quad 1 < p < 2 \quad (6)$$

and taking $p \rightarrow 1$. The main advantage of this formulation is that it is strictly convex. We first show that $J_{p,R}$ converges to $J_{1,R}$ as $p \rightarrow 1$. For this it is sufficient to show

Lemma 1.

$$\lim_{p \rightarrow 1} \frac{1}{p} \int_{\Omega} |\nabla u|^p = \int_{\Omega} |\nabla u|. \quad (7)$$

Proof. See [27]. \square

Remark 1. As $J_{p,R}(\mathbf{u}) \rightarrow J_{1,R}(\mathbf{u})$ as $p \rightarrow 1$, the corresponding Euler-Lagrange equations $A_p = \Delta_p$ associated with the regularization term also converges to $A_1 = \Delta_1$.

Observe that if $\alpha = 0$, i.e. in the absence of the regularization term, one can directly apply the CR operator

$$R = \begin{bmatrix} \partial_y & -\partial_x \\ \partial_x & \partial_y \end{bmatrix}.$$

to decouple the system to obtain a degenerate system:

$$\begin{cases} \frac{\partial \xi}{\partial t} = 0, \\ \frac{\partial \zeta}{\partial t} = \beta \Delta(\phi(f)\zeta). \end{cases} \quad (8)$$

where $\xi = u_y - v_x$ and $\zeta = k(u_x + v_y)$. The first equation means the vorticities will remain unchanged. On the other hand, for the divergence equation, we have a degeneracy at the null values of the image function f . Thus, as expected by the aperture problem, this leads to an ill-posed problem. We now study the associated parabolic system:

$$\begin{cases} \frac{\partial u}{\partial t} = \Delta_p u + a_0 \frac{\partial}{\partial x} [\phi(f)(u_x + v_y)] \text{ in } \Omega \times (0, \infty), \\ \frac{\partial v}{\partial t} = \Delta_p v + a_0 \frac{\partial}{\partial y} [\phi(f)(u_x + v_y)] \text{ in } \Omega \times (0, \infty), \\ u(x, y, 0) = u_0 \text{ in } \Omega, \\ v(x, y, 0) = v_0 \text{ in } \Omega, \\ \frac{\partial u}{\partial n} = 0 \text{ on } \partial\Omega \times (0, \infty), \\ \frac{\partial v}{\partial n} = 0 \text{ on } \partial\Omega \times (0, \infty), \end{cases} \quad (9)$$

where (u_0, v_0) is the starting feasible solution obtained by the Horn and Schunck optical flow, $a_0 = 2\beta/\alpha$. We study the problem (9) using an evo-

lutionary PDE approach. In abstract form the system (9) can be written as

$$\begin{cases} \frac{d\mathbf{u}}{dt} + \mathcal{A}_p \mathbf{u} = 0, & t > 0, \\ \mathbf{u}(0) = \mathbf{u}_0 \in H^1(\Omega)^2. \end{cases} \quad (10)$$

Here the operator $\mathcal{A}_p = A_p + F$ where

$$A_p \mathbf{u} = - \begin{bmatrix} \Delta_p u \\ \Delta_p v \end{bmatrix}, \quad F \mathbf{u} = -a_0 \begin{bmatrix} \frac{\partial}{\partial x} [\phi(f)(u_x + v_y)] \\ \frac{\partial}{\partial y} [\phi(f)(u_x + v_y)] \end{bmatrix},$$

The operator A_p is maximal monotone in $W^{1,p}(\Omega) \cap L^2(\Omega)$, see [37]. We now show that the operator F is maximal monotone in $L^2(\Omega)$.

Lemma 2. The operator F is maximal monotone in $L^2(\Omega)$.

Proof. To show monotonicity we show that $\langle F\mathbf{u}, \mathbf{u} \rangle \geq 0$. Indeed,

$$\begin{aligned} \langle F\mathbf{u}, \mathbf{u} \rangle &= -a_0 \int_{\Omega} \left\{ \frac{\partial}{\partial x} [\phi(f)(u_x + v_y)] u + \frac{\partial}{\partial y} [\phi(f)(u_x + v_y)] v \right\}, \\ &= a_0 \int_{\Omega} \{ \phi(f)(u_x + v_y) u_x + \phi(f)(u_x + v_y) v_y \}, \\ &= a_0 \int_{\Omega} \phi(f)(u_x + v_y)^2 \geq 0, \end{aligned}$$

showing that F is monotone. To show maximal monotonicity we have to show that $R(I + F) = H$. Here $H = L^2(\Omega)$. Consider the system

$$\begin{aligned} u + \frac{\partial}{\partial x} [\phi(f)(u_x + v_y)] &= f, \\ v + \frac{\partial}{\partial y} [\phi(f)(u_x + v_y)] &= g, \end{aligned}$$

where $f, g \in L^2(\Omega)$. Applying the Cauchy-Riemann operator

$$R = \begin{bmatrix} \partial_y & -\partial_x \\ \partial_x & \partial_y \end{bmatrix}.$$

both sides we obtain the decoupled system

$$u_y - v_x = f_y - g_x,$$

$$\Delta(k(u_x + v_y)) = f_x + g_y,$$

where $k = 1 + a_0\phi(f)$. The second equation is first solved for $k(u_x + v_y)$. Let us call this solution h_2 . Let us also define $h_1 = f_y - g_x$. We thus obtain the following system

$$\begin{aligned} u_y - v_x &= h_1, \\ u_x + v_y &= h_2/k, \end{aligned}$$

These are the inhomogeneous Cauchy-Riemann equations which can be solved uniquely. This concludes the proof. \square

Let us finally define a function $\Phi : L^2(\Omega)^2 \rightarrow (-\infty, +\infty]$ by

$$\Phi(\mathbf{u}) = \begin{cases} J_{p,\mathbf{R}}(\mathbf{u}), & \mathbf{u} \in [W^{1,p}(\Omega) \cap L^2(\Omega)]^2 \\ +\infty, & \mathbf{u} \in [L^2(\Omega) \setminus W^{1,p}(\Omega)]^2 \end{cases}.$$

Then clearly Φ is convex and lower semi-continuous. Also Φ is proper since $D(\Phi) = D(A_p) \cap D(F) \neq \emptyset$. Thus the associated subdifferential $\partial\Phi(\mathbf{u}) \equiv \mathcal{A}_p$ is maximal monotone. Thus there is a unique solution \mathbf{u} of the inclusion

$$0 \in \mathbf{u}'(t) + \partial\Phi(\mathbf{u})$$

satisfying the initial condition.

2.3 Approximating the CEC based Model

In this section we show that for a specific choice of the additional constraint our model closely approximates the CEC based model. To establish this we first consider the two constrained optimization problem and their associated augmented Lagrangian framework. Consider the CEC based model with non-quadratic regularization:

$$\min_{\mathbf{v}} J_C(\mathbf{v}) = \int_{\Omega} (f_t + \nabla \cdot (f\mathbf{v}))^2 + \alpha \int_{\Omega} (|\nabla \bar{u}| + |\nabla \bar{v}|), \quad (11)$$

subject to the constraint

$$B\mathbf{v} := \nabla f \cdot \mathbf{v} = -f_t =: c. \quad (12)$$

where $\mathbf{v} = (\bar{u}, \bar{v})$ and α is the regularization parameter. For simplicity in computation throughout this section we fix $\beta = 1, \phi(f) = f^2, \psi = (\nabla \cdot \mathbf{u})^2$.

Let us denote the function spaces $V = H^1(\Omega) \times H^1(\Omega)$ and $H = L^2(\Omega)$. For the purpose of analysis we replace the bounded constraint with an equality constraint. We now consider the augmented Lagrangian $\mathcal{L}_{\tilde{\mu}} : V \times H \rightarrow \mathbb{R}$, $\mu > 0$ for the problem (11)-(12) defined as:

$$\mathcal{L}_{\tilde{\mu}}(\mathbf{v}, \lambda_1) = J_1(\mathbf{v}) + \frac{\tilde{\mu}}{2} \|B\mathbf{v} - c\|^2 + \langle \lambda_1, B\mathbf{v} - c \rangle. \quad (13)$$

The associated constrained optimization problem of our model is

$$J_{1,R}(\mathbf{v}) = \int_{\Omega} f^2(\nabla \cdot \mathbf{v})^2 + \alpha \int_{\Omega} (|\nabla \bar{u}| + |\nabla \bar{v}|), \quad (14)$$

subject to the constraint

$$B\mathbf{v} = c. \quad (15)$$

The associated Augmented Lagrangian then becomes

$$\mathcal{L}_{\mu}(\mathbf{v}, \lambda_1) = J_{1,R}(\mathbf{v}) + \frac{\mu}{2} \|B\mathbf{v} - c\|^2 + \langle \lambda_1, B\mathbf{v} - c \rangle. \quad (16)$$

Definition 1. A point (\mathbf{u}, λ) is said to be a saddle point of (13) if

$$\mathcal{L}_{\tilde{\mu}}(\mathbf{u}, \lambda_1) \leq \mathcal{L}_{\tilde{\mu}}(\mathbf{u}, \lambda) \leq \mathcal{L}_{\tilde{\mu}}(\mathbf{v}, \lambda) \quad \forall (\mathbf{v}, \lambda_1) \in V \times H. \quad (17)$$

Lemma 3. (\mathbf{u}, λ) is a saddle point of (13) iff \mathbf{u} solves the variational problem (11)-(12).

Proof. Let \mathbf{u} solve the variational problem (11)-(12). Then

$$\mathcal{L}_{\tilde{\mu}}(\mathbf{u}, \lambda_1) = \mathcal{L}_{\tilde{\mu}}(\mathbf{u}, \lambda).$$

since $B\mathbf{u} = c$. Also $J_{1,R}(\mathbf{u}) \leq J_{1,R}(\mathbf{v})$ for all \mathbf{v} since \mathbf{u} solves (11). This leads to the second inequality

$$\mathcal{L}_{\tilde{\mu}}(\mathbf{u}, \lambda) \leq \mathcal{L}_{\tilde{\mu}}(\mathbf{v}, \lambda).$$

Conversely assume that (17) holds. Then by the first inequality we have

$$\langle \lambda_1, B\mathbf{u} - c \rangle \leq \langle \lambda, B\mathbf{u} - c \rangle \quad \text{implies} \quad \langle \lambda_1 - \lambda, B\mathbf{u} - c \rangle \leq 0,$$

from which we conclude $B\mathbf{u} = c$. From the second inequality we have

$$J_C(\mathbf{u}) + \frac{\tilde{\mu}}{2} \|B\mathbf{u} - c\|^2 + \langle \lambda, B\mathbf{u} - c \rangle \leq J_C(\mathbf{v}) + \frac{\tilde{\mu}}{2} \|B\mathbf{v} - c\|^2 + \langle \lambda, B\mathbf{v} - c \rangle,$$

for all $\mathbf{v} \in V$. We make a change of variable $\mathbf{v} = \mathbf{u} + t(\mathbf{w} - \mathbf{u})$ for all $\mathbf{w} \in V$

and $0 \leq t \leq 1$. Now

$$\begin{aligned} \langle \lambda, B\mathbf{v} - c \rangle - \langle \lambda, B\mathbf{u} - c \rangle &= \langle \lambda, B(\mathbf{u} + t(\mathbf{w} - \mathbf{u})) - c \rangle - \langle \lambda, B\mathbf{u} - c \rangle \\ &= \langle \lambda, B(\mathbf{u} + t(\mathbf{w} - \mathbf{u})) - c - B\mathbf{u} + c \rangle \\ &= t\langle \lambda, B(\mathbf{w} - \mathbf{u}) \rangle. \end{aligned} \quad (18)$$

Similarly

$$\begin{aligned} \frac{\tilde{\mu}}{2}\|B\mathbf{v} - c\|^2 - \frac{\tilde{\mu}}{2}\|B\mathbf{u} - c\|^2 &= \frac{\tilde{\mu}}{2}\|B(\mathbf{u} + t(\mathbf{w} - \mathbf{u})) - c\|^2 - \frac{\tilde{\mu}}{2}\|B\mathbf{u} - c\|^2 \\ &= \frac{\tilde{\mu}t^2}{2}\|B(\mathbf{w} - \mathbf{u})\|^2. \end{aligned} \quad (19)$$

Finally combining the terms we obtain

$$J_C(\mathbf{u} + t(\mathbf{w} - \mathbf{u})) - J_C(\mathbf{u}) + t\langle \lambda, B(\mathbf{w} - \mathbf{u}) \rangle + \frac{\tilde{\mu}t^2}{2}\|B(\mathbf{w} - \mathbf{u})\|^2 \geq 0.$$

By convexity of J_C we get

$$t(J_C(\mathbf{w}) - J_C(\mathbf{u})) + t\langle \lambda, B(\mathbf{w} - \mathbf{u}) \rangle + \frac{\tilde{\mu}t^2}{2}\|B(\mathbf{w} - \mathbf{u})\|^2 \geq 0.$$

Dividing throughout by t and taking limit as $t \rightarrow 0$ we obtain

$$J_C(\mathbf{w}) - J_C(\mathbf{u}) + \langle \lambda, B(\mathbf{w} - \mathbf{u}) \rangle \geq 0 \quad \forall \mathbf{w} \in V \text{ and } \lambda \in H. \quad (20)$$

Consequently \mathbf{u} solves the variational problem (11). \square

Lemma 4. The tuple (\mathbf{u}, λ) is also the saddle point of the unconstrained optimization problem (16).

Observe that the augmented Lagrangian (13) can be reformulated as

$$\mathcal{L}_{\tilde{\mu}}(\mathbf{v}, \lambda_1) = J(\mathbf{v}) + \frac{\tilde{\mu}}{2}\|B\mathbf{v} - c\|^2 + \langle \lambda_1 + 2f\nabla \cdot \mathbf{v}, B\mathbf{v} - c \rangle. \quad (21)$$

The parameter $\tilde{\mu}$ can be chosen as large as necessary. The unknown λ_1 is obtained by the Uzawa iteration

$$\lambda_1^{(n+1)} = \lambda_1^{(n)} + 2fd^{(n)} + \rho^{(n)}(B\mathbf{v}^{(n)} - c), \quad (22)$$

where $d^{(n)} = \nabla \cdot \mathbf{v}^{(n)}$. For the Uzawa iterations to converge it is necessary that the terms $d^{(n)}$ remain bounded. In general it is not known whether this term is bounded, but the diffusion phenomena ensures boundedness in this case.

We demonstrate this idea by the bounded constraint algorithm described below. But first we show the convergence of the Uzawa iterations.

Theorem 1. The Uzawa iterations $\lambda_i^{(n)}$ converge as $n \rightarrow \infty$.

Proof. Set $n = i$ in Equation (22)

$$\lambda_1^{(i+1)} - \lambda_1^{(i)} = 2fd^{(i)} + \rho^{(i)}(B\mathbf{v}^{(i)} - c), \quad 1 \leq i \leq n.$$

Adding the n equations we obtain

$$\lambda_1^{(n+1)} - \lambda_1^{(0)} = 2f \sum_{i=0}^n d^{(i)} + \sum_{i=0}^n \rho^{(i)}(B\mathbf{v}^{(i)} - c).$$

Hence

$$\|\lambda_1^{(n+1)} - \lambda_1^{(0)}\|_{L^2} \leq 2\|f\| \sum_{i=0}^n \|d^{(i)}\|_{L^2} + \sum_{i=0}^n |\rho^{(i)}| \|B\mathbf{v}^{(i)} - c\|_{L^2}. \quad (23)$$

The second term in (23) is bounded. In fact we can show

$$\sum_{i=0}^n |\rho^{(i)}| \|B\mathbf{v}^{(i)} - c\|_{L^2} \leq r,$$

where

$$r = \max \left\{ \frac{\pi^2}{6} mCM, 2\delta_{\text{HS}} \right\}.$$

See [16] for the details. Since Ω is bounded, to show boundedness of $d^{(i)}$ it is sufficient to show that the iterates $\mathbf{v}^{(i)}$ remain bounded. In this context we make use of Lemma 3.1 from [8] which discusses boundedness for the OFC case. We extend it for the continuity equation case.

Lemma 5. Let Ω be open and bounded, $f_t \in L^2(\Omega)$, $f_x, f_y \in L^\infty(\Omega)$ such that they are linearly independent. Let $\mathbf{v}^{(n)}$ be a sequence in $L^p(\Omega)$. If there exists a sequence of vectors $c^{(n)}$ in \mathbb{R}^2 such that $c^{(n)} + \mathbf{v}^{(n)}$ is bounded in $L^p(\Omega)$ and $\|f_t + \nabla \cdot (f\mathbf{v}^{(n)})\|_{L^p}$ is bounded in $L^p(\Omega)$, then $\mathbf{v}^{(n)}$ is bounded in $L^p(\Omega)$.

Proof. It is sufficient to show that $c^{(n)}$ is bounded in $L^p(\Omega)$. Assume on the contrary that $c^{(n)}$ is unbounded. Then there is a subsequence (call it $c^{(n)}$ again) such that $|c^{(n)}|$ diverges. Then $\frac{c^{(n)}}{|c^{(n)}|}$ is a bounded sequence. By Bolzano-Weierstrass theorem it has a subsequence $g^{(n)}$ such that $g^{(n)} \rightarrow g$, where $|g| = 1$. But then

Algorithm 1 Bounded Constraint Algorithm

```

1: procedure BCA
2:   Set  $\lambda^{(0)}, \rho^{(0)}$ . Choose  $\epsilon_1^{(0)}, \epsilon_2^{(0)}$ .
3:   Obtain initial HS optical flow  $\mathbf{v}^{(0)}$ 
4:   for  $n = 1, 2, \dots$  until convergence do
5:     update  $\mathbf{v}^{(n)}, d^{(n)}$ 
6:     if  $\|B\mathbf{v}^{(n)} - c\| \leq \max\{\epsilon_1^{(n)}, 2\delta_{\text{HS}}\}$ 
7:       if  $\|fd^{(n)}\| \leq \epsilon_2^{(n)}$ 
8:         break;
9:       else
10:        update  $\lambda_1^{(n)}$  by (22)
11:         $\rho^{(n+1)} \leftarrow \rho^{(n)}$ 
12:         $\epsilon_1^{(n+1)} \leftarrow \epsilon_1^{(n)} / \rho^{(n+1)0.9}$ 
13:         $\epsilon_2^{(n+1)} \leftarrow \epsilon_2^{(n)} / \rho^{(n+1)}$ 
14:      else
15:        update  $B\mathbf{v}^{(n)} - c$ 
16:         $\lambda^{(n+1)} \leftarrow \lambda^{(n)}$ 
17:         $\rho^{(n+1)} \leftarrow 100\rho^{(n)}$ 
18:         $\epsilon_1^{(n+1)} \leftarrow \epsilon_1^{(n)} / \rho^{(n+1)0.1}$ 
19:         $\epsilon_2^{(n+1)} \leftarrow \epsilon_2^{(n)} / \rho^{(n+1)}$ 

```

$$\begin{aligned} \|f_t + \nabla \cdot (f\mathbf{v}^{(n)})\|_{L^p} &= \|f_t + \nabla \cdot (f(c^{(n)} + \mathbf{v}^{(n)})) - \nabla \cdot (fc^{(n)})\|_{L^p} \\ &\geq \|\nabla \cdot (fc^{(n)})\|_{L^p} - \|f_t + \nabla \cdot (f(c^{(n)} + \mathbf{v}^{(n)}))\|_{L^p} \end{aligned}$$

implies that $\nabla \cdot (fc^{(n)})$ is bounded. Now $\nabla \cdot (fc^{(n)}) = \nabla f \cdot c^{(n)} + f\nabla \cdot c^{(n)}$. The second term is zero. By our hypothesis $\nabla f \cdot g^{(n)} \rightarrow 0$ in $L^p(\Omega)$. But then by continuity of norms we have $\|\nabla f \cdot g\|_{L^p} = 0$ contradicting linear independence of f_x and f_y . This completes the proof. \square

Coming back to the proof, combining the above lemma we can choose a N such that for $i > N$ we have

$$\|d^{(i)}\| \leq \frac{1}{(i+1)^2}$$

so that

$$\|\lambda_1^{(n+1)} - \lambda_1^{(0)}\|_{L^2} \leq 2\|f\| \sum_{i=0}^n \frac{1}{(i+1)^2} + r$$

which remains finite. This completes the proof. \square

We now describe the bounded constraint algorithm (1). The algorithm can be realized in two phases. The first phase comprises of the steps (7-13). This happens when the criterion (6) is met. In other words, the iterates $\mathbf{v}^{(n)}$ actually satisfy the OFC upto a tolerance threshold. This phase is diffusion-driven. The algorithm terminates when the criterion (7) is met as it guarantees the convergence of the iterates $\lambda^{(n)}$. Otherwise the updates happen by the Uzawa iterations through steps (10-13). We reach the second phase if the convergence criteria (6) is not met. Here the bounded constraint is first updated. This updation approximates the continuity equation constraint because OFC is already embedded in it. Also to prevent any erroneous update the Lagrange multiplier is assigned the value from it's previous iteration. In either phases the tolerance limits are tightened so that it doesn't fall rapidly.

3 Numerical Discretization and Results

In this section we present the discretization details of our algorithm. We also show the results obtained by our algorithm on different datasets comparing our results with the continuity equation model. We further demonstrate how our model can be adapted to rigid motion estimation by showing results on the sphere sequence. To show the robustness of L^1 regularization we discuss the behaviour of our model under the effect of noise. For all practical purposes we assume that $f \in W^{1,\infty}(\Omega)$, i.e. f is Lipschitz continuous. Such a choice is natural in image processing as images are usually pre-processed before applying the algorithm. Also $f_x, f_y \in L^\infty(\Omega)$ such that they are linearly independent. Theoretically this condition is needed to ensure coercivity of the bilinear form associated with the HS model [35]. Numerically this may not hold for some synthetic images, for example, sequences which have only unidirectional motion. However for most of the real-world sequences the assumption holds.

We now consider the E-L equations associated with our refinement functional (5) given by:

$$\begin{cases} \Delta_1 u + a_0 \frac{\partial}{\partial x} [\phi(f)(u_x + v_y)] = 0 \\ \Delta_1 v + a_0 \frac{\partial}{\partial y} [\phi(f)(u_x + v_y)] = 0, \end{cases} \quad (24)$$

In expanded form the 1–laplacian is written as

$$\Delta_1 u = \frac{u_{xx}u_y^2 - 2u_xu_yu_{xy} + u_{yy}u_x^2}{(u_x^2 + u_y^2)^{3/2}}.$$

Let us define the forward difference operators by

$$\Delta_x^+ u = \frac{u_{i+1,j} - u_{i,j}}{dx}, \quad \Delta_y^+ u = \frac{u_{i,j+1} - u_{i,j}}{dy}.$$

For higher order derivatives we again use the standard finite difference operators

$$\begin{aligned} \Delta_{xx} u &= \frac{u_{i+1,j} + u_{i-1,j} - 2u_{i,j}}{dx^2}, & \Delta_{yy} u &= \frac{u_{i,j+1} + u_{i,j-1} - 2u_{i,j}}{dy^2}, \\ \Delta_{xy} u &= \frac{u_{i+1,j+1} - u_{i+1,j-1} - u_{i-1,j+1} + u_{i-1,j-1}}{4 dx dy}. \end{aligned}$$

The discretization of 1–laplacian operator thus become

$$\Delta_1^D u \approx \frac{\Delta_{xx} u (\epsilon^2 + (\Delta_y^+ u)^2) - 2\Delta_x^+ u \Delta_y^+ u \Delta_{xy} u + \Delta_{yy} u (\epsilon^2 + (\Delta_x^+ u)^2)}{(\epsilon^2 + (\Delta_x^+ u)^2 + (\Delta_y^+ u)^2)^{3/2}}.$$

A small constant $\epsilon > 0$ is introduced to avoid singularities of the operator at origin. Let us also define the discrete divergence operator

$$D^+ = \Delta_x^+ + \Delta_y^+.$$

The system of equations (24) in discretized form thus becomes

$$\begin{bmatrix} \frac{2\beta f^2}{\Delta x^2} & 0 \\ 0 & \frac{2\beta f^2}{\Delta y^2} \end{bmatrix} \begin{bmatrix} u^{(n+1)} \\ v^{(n+1)} \end{bmatrix} = \begin{bmatrix} \alpha \Delta_1^D u^{(n)} + \beta \Delta_x^+ [f^2 D^+ \cdot \mathbf{u}^{(n)}] \\ \alpha \Delta_1^D v^{(n)} + \beta \Delta_y^+ [f^2 D^+ \cdot \mathbf{u}^{(n)}] \end{bmatrix}, \quad (25)$$

In [7], the authors discuss topology-preserving linear filtering techniques applied to medical images. In image processing PDEs govern the local interaction of neighboring pixels. As a result filtering techniques are useful approximations which are computationally easier. However complicated geometric structures in images pose a challenge for efficient filter design to recover and extract important features. To cope with this difficulty the authors proposed a linearized approximation depending on the initial data. There are several advantages to this approach. Computationally it is

simpler and efficient since application of filter on the initial data is done in the beginning and are not computed again at each iteration. Additionally the linearized version has a direct knowledge of the data and acts as a fidelity term. Using this idea in our context we are led to the following scheme

$$\begin{bmatrix} \frac{2\beta f^2}{\Delta x^2} & 0 \\ 0 & \frac{2\beta f^2}{\Delta y^2} \end{bmatrix} \begin{bmatrix} u^{(n+1)} \\ v^{(n+1)} \end{bmatrix} = \begin{bmatrix} \alpha \Delta_1^L u_0 + \beta \Delta_x^+ [f^2 D^+ \cdot \mathbf{u}^{(n)}] \\ \alpha \Delta_1^L v_0 + \beta \Delta_y^+ [f^2 D^+ \cdot \mathbf{u}^{(n)}] \end{bmatrix}, \quad (26)$$

where $\Delta_1^L u_0 = \Delta_1^D u_0$ (similarly v_0). This quantity is fixed and does not change over iterations. An useful approximation of Δ_1 is discussed in [31] where the author present an explicit convergent monotone scheme for motion of level sets by mean curvature given as

$$\Delta_1 u \approx 2 \frac{u(x) - u_*}{dx^2} + \mathcal{O}(dx^2 + d\theta), \quad (27)$$

where $u(x)$ is the value at the centre of the grid, u_* denotes the median value of the neighbors in the grid, dx is the spatial resolution and $d\theta$ is the directional resolution. For images, which have a natural discrete structure $d\theta$ is fixed at $\pi/4$. The main advantage of this approximation scheme is that it is monotone. This means that discrete comparison principle holds. More details on this scheme can be found in [31]. Using this approximation we have the following scheme:

$$\begin{bmatrix} \frac{2\beta f^2}{\Delta x^2} + \alpha & 0 \\ 0 & \frac{2\beta f^2}{\Delta y^2} + \alpha \end{bmatrix} \begin{bmatrix} u^{(n+1)} \\ v^{(n+1)} \end{bmatrix} = \begin{bmatrix} \alpha \text{med}(u) + \beta \Delta_x^+ [f^2 D^+ \cdot \mathbf{u}^{(n)}] \\ \alpha \text{med}(v) + \beta \Delta_y^+ [f^2 D^+ \cdot \mathbf{u}^{(n)}] \end{bmatrix}, \quad (28)$$

where $\text{med}(u)$ denotes the median value of the surrounding pixels. All these numerical schemes start with the initialization (u_0, v_0) which is the HS optical flow. Hence forth, we refer to our constraint-based refinement flow field with quadratic regularization [16] as $L^2 - L^2$ approach and the refinement process in the current work with L^1 regularization as $L^2 - L^1$ approach. We call the refinement using linearized approximation using the initial data as linearized $L^2 - L^1$ approach.

We start with the Oseen vortex sequence and consider the case where $\phi(f) = f^2$ and $\psi = (\nabla \cdot \mathbf{u})^2$. The Oseen vortex pair is a synthetic PIV sequence of dimension 500×500 . The vorticies are placed centered at the

positions $(166.7, 250)$ and $(333.3, 250)$. The circumferential velocity is given by $v_\theta = (\Gamma/2\pi r)[1 - \exp(-r^2/r_0^2)]$ with the vortex strength $\Gamma = \pm 7000$ pixels²/s and vortex core radius $r_0 = 15$ pixels. For more details see [24].

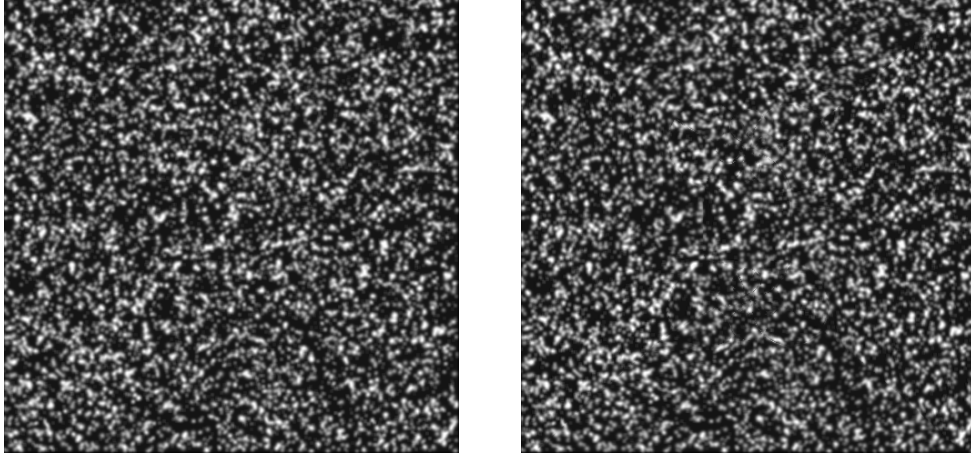


Figure 1: Oseen vortex pairs.

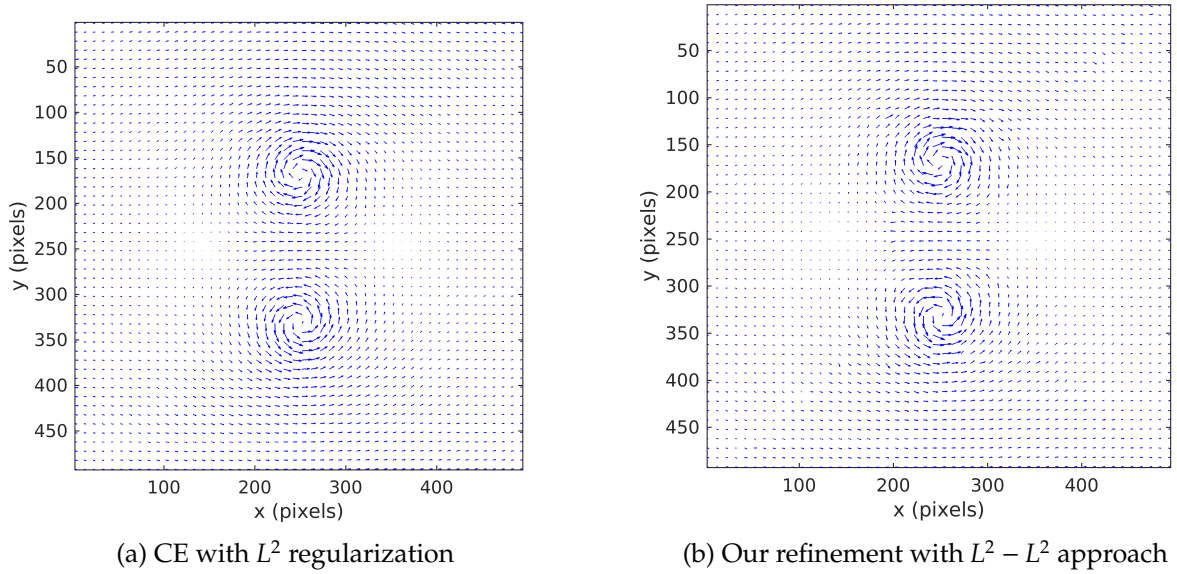
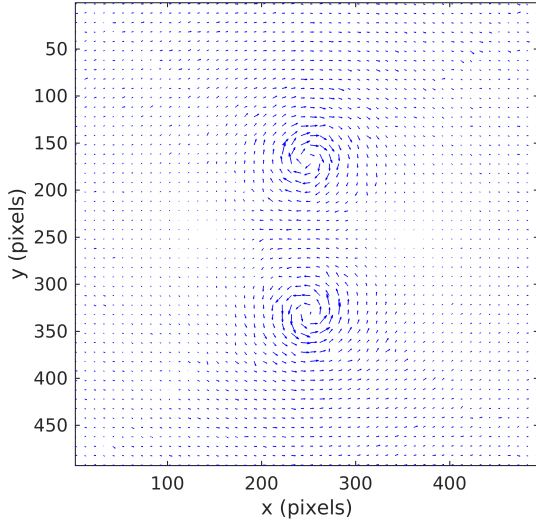
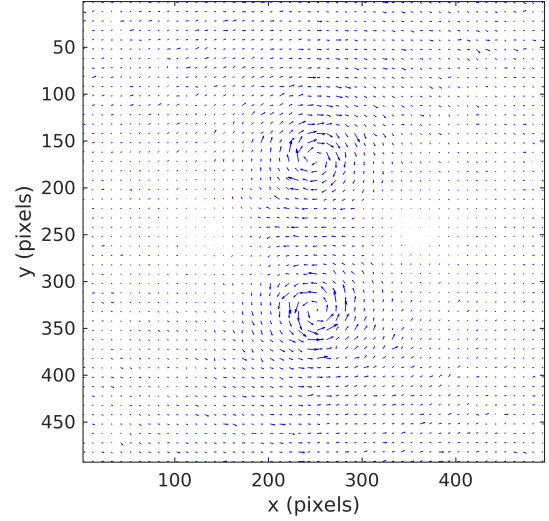


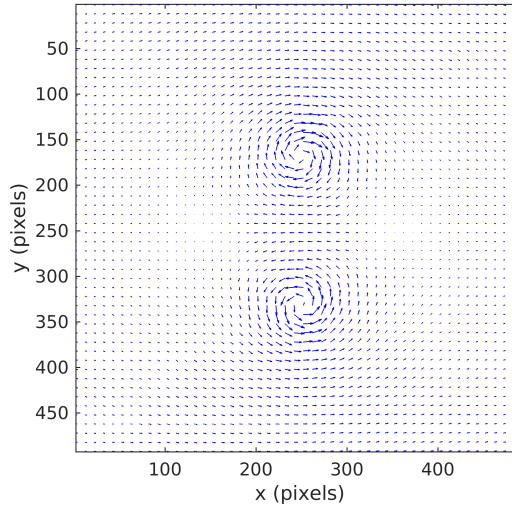
Figure 2: Vorticity plots for the Oseen vortex pair



(a) Our refinement with $L^2 - L^1$ approach



(b) Our refinement with linearized $L^2 - L^1$ approach



(c) Our refinement with median filtering

Figure 3: Vorticity field of the Oseen vortex pairs.

Figure (2a) shows the vorticity field of the continuity equation model with L^2 regularization for the oseen vortex pair after 100 iterations. Figure (2b) shows our refinement algorithm using the $L^2 - L^2$ approach. Figures (3a) and (3b) show our refinement obtained by solving systems (25) and (26) respectively after 15 iterations. We have chosen $\alpha = 1, \beta = 0.01$ and $\epsilon = 0.1$. For the filtering approximations the value of α was chosen to be 100. In this case it was observed experimentally that the numerical scheme converges when the ratio β/α is less than or equal to 10^{-4} . Figure (28) shows the refinement with the median filtering approximation. To compare the results we avoid the Liu-Shen coarse-to-fine structure for the continuity

model since our refinement process implementation pertains only to one stage. One does not observe much difference between the vorticity fields in Figure (2b) and Figure (3c) because of the HS initialization which is a divergence-free approximation of the continuity equation model.

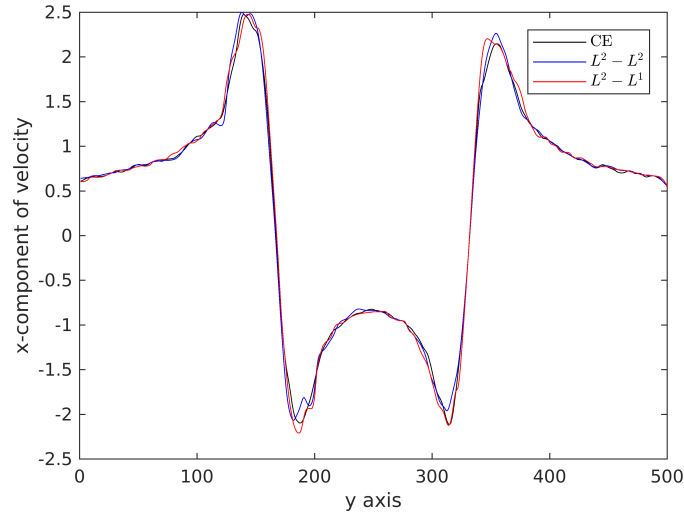


Figure 4: Comparison of the distributions of x -component of the velocity field for the oseen vortex pair obtained for Figures (2a), (2b) and (3c).

Figure (3) shows the distribution of the x -component of the velocity for the oseen vortex pair. This clearly shows the closeness of both the approaches with the continuity equation model. A slight deviation is observed between the plots near the vortex cores. This further highlights the effect of isotropic initialization on the refinement phenomena. We now show the result for the $L^1 - L^1$ approach.

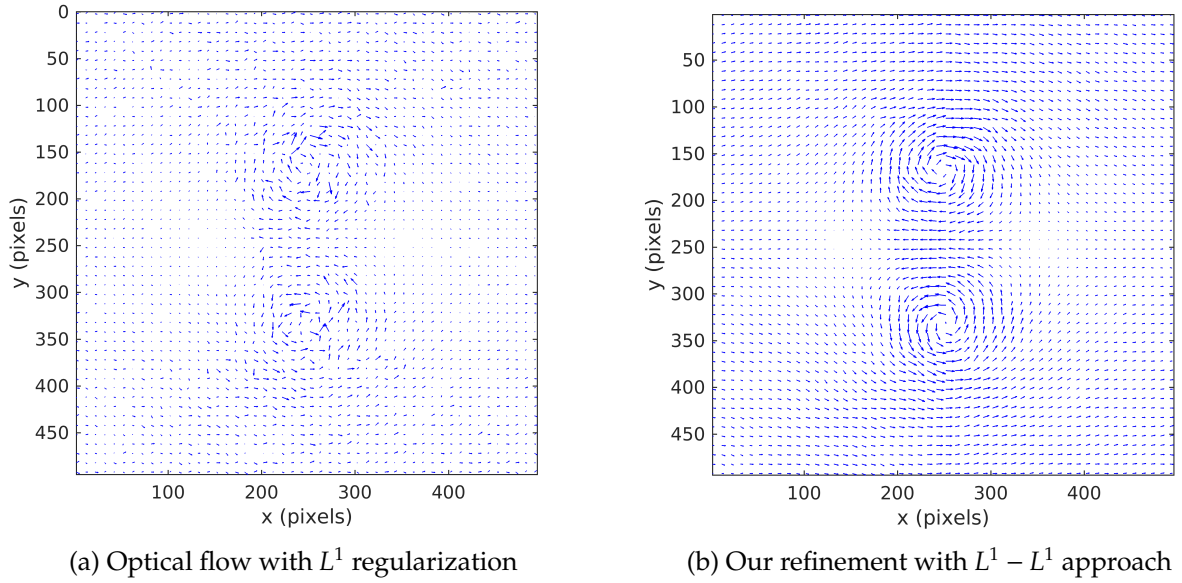


Figure 5: The refinement process with the $L^1 - L^1$ approach.

The situation is very different in the $L^1 - L^1$ approach. Here the initialization is the optical flow field obtained as a minimization with L^1 regularization. Unlike the HS initialization, this does not provide a good starting solution for the refinement process specially for fluid flow sequences as shown in Figure (5a). Figure (5b) shows the corresponding vorticity plot. The density of vectors occur mainly near the vortex cores.

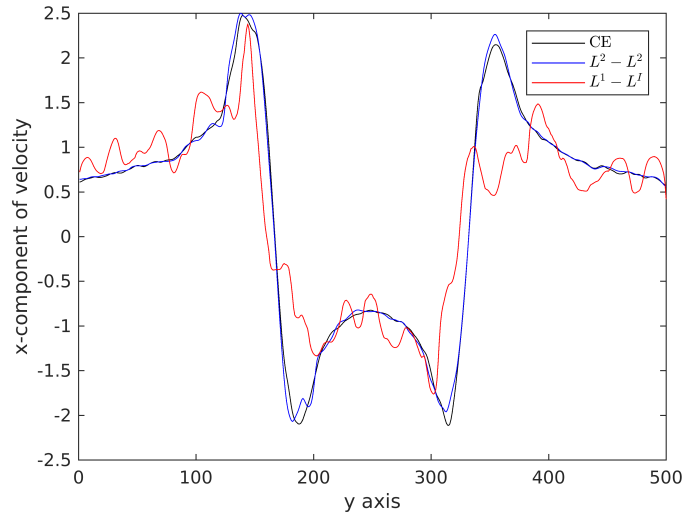


Figure 6: Comparison of the distributions of x -component of the velocity field for the oseen vortex pair.

Figure (6) clearly highlights the difference between the two approaches. In the $L^1 - L^1$ approach the peaks are smaller compared to the $L^2 - L^2$

approach. This is because of the anisotropic diffusion of the Δ_1 operator which diffuses only within the level sets and not across them. The plots further indicate that this approach is not ideal for fluid-flow estimation. We now discuss the case when the images are corrupted with noise. The results are shown for the oseen vortex pair.

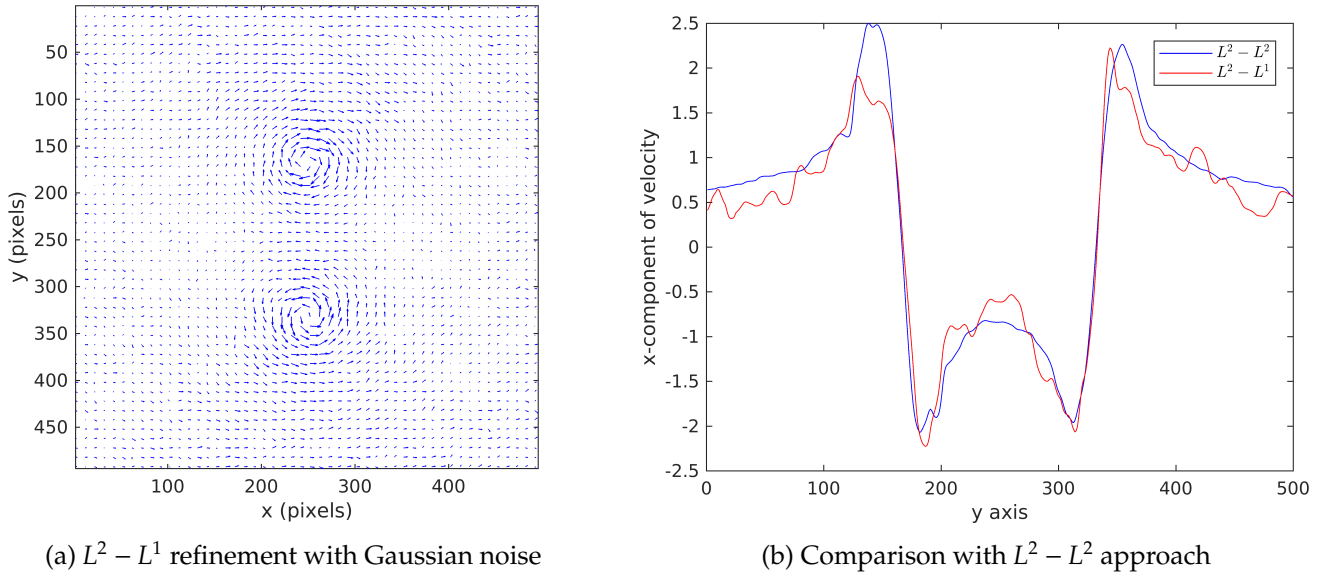


Figure 7: Behaviour of the model under Gaussian noise.

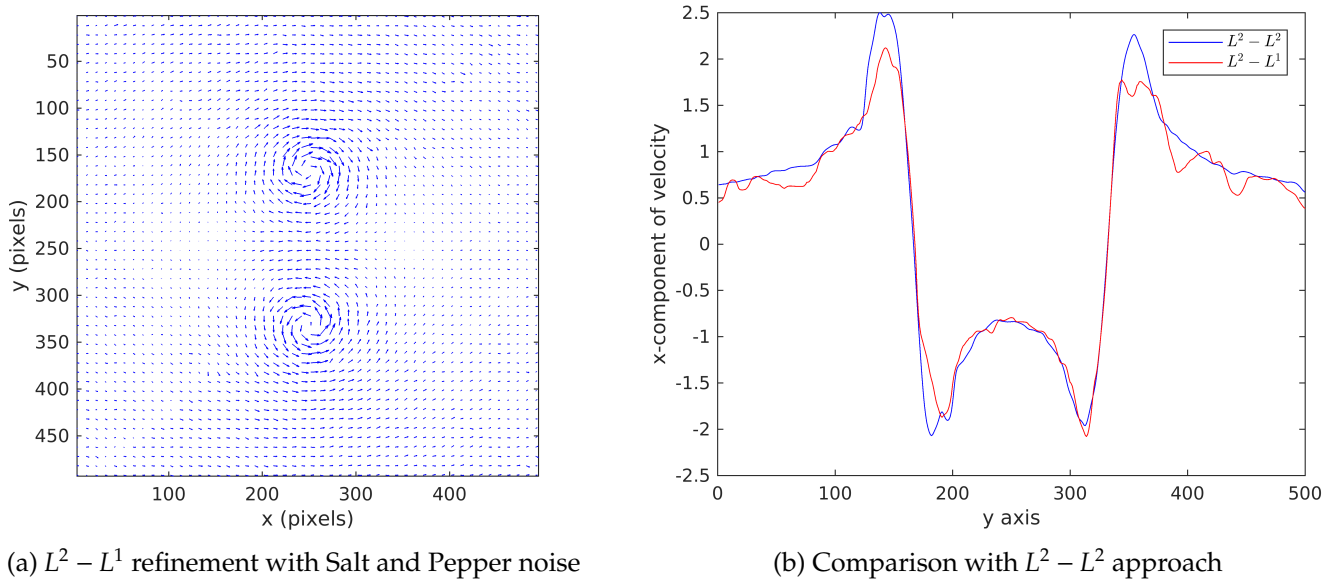


Figure 8: Behaviour of the model under Salt and Pepper noise.

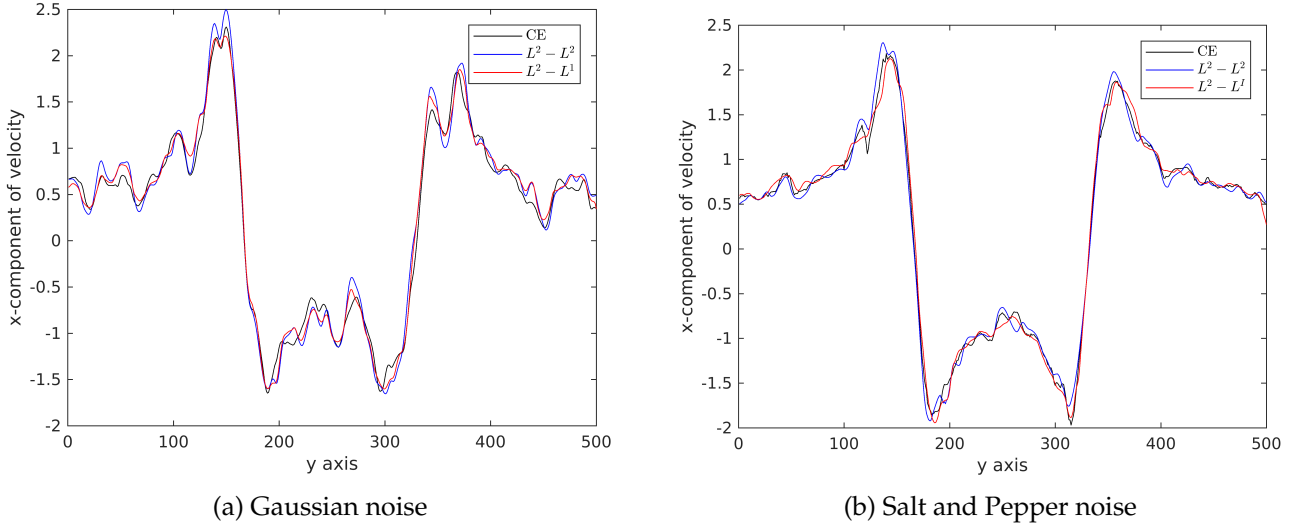


Figure 9: Behaviour of all the three approaches under noise.

Figure (7a) shows the vorticity plot for the $L^2 - L^1$ approach on the oseen vortex pair where the underlying image frames have been corrupted with 10% Gaussian noise and Figure (7b) show the comparison of the x -component distribution with the $L^2 - L^2$ approach without noise. The plots indicate that the vortex cores appear slightly flatter rather than circular. Most of the spatial characteristics of the flow have been retained except for certain distortions near the end. Figure (8a) shows a similar plot under the application of salt and pepper noise. As median filters are known to remove salt and pepper noise from digital images, the robustness of our refinement model is clearly seen when compared to the $L^2 - L^2$ approach without noise. Figure (9) compares the distribution of the x -component of velocity of all the three approaches under noise. We now show the results for the cloud sequence. The distribution of the strength of the vortices in the cloud sequence obeys a Gaussian distribution of mean 0 and standard deviation of $3000 \text{ (pixels)}^2/\text{s}$.

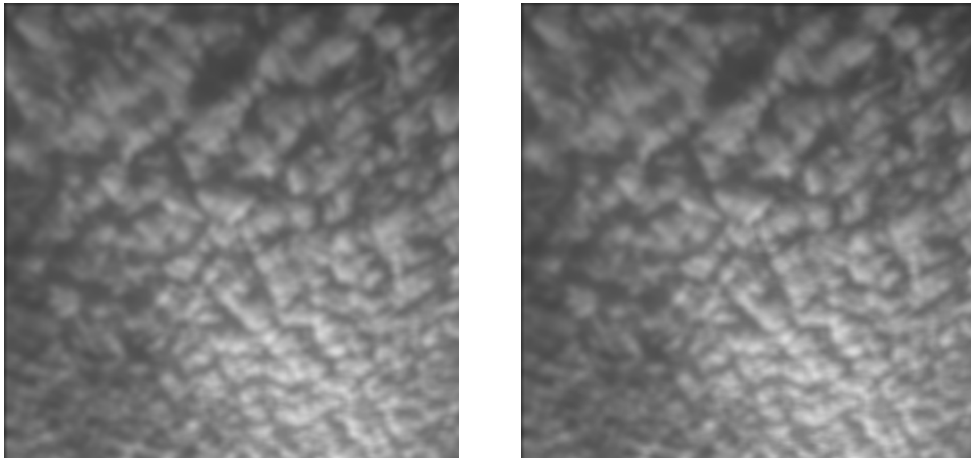
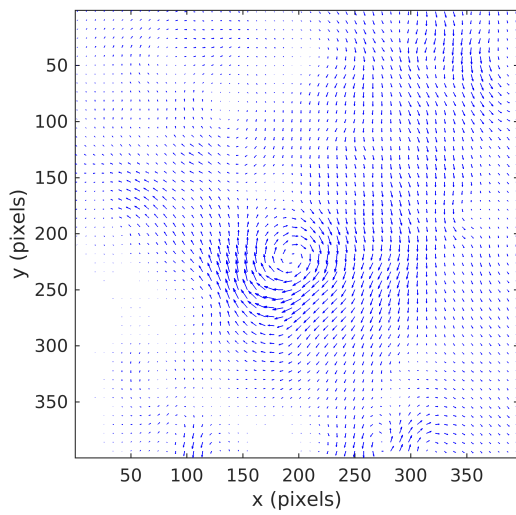
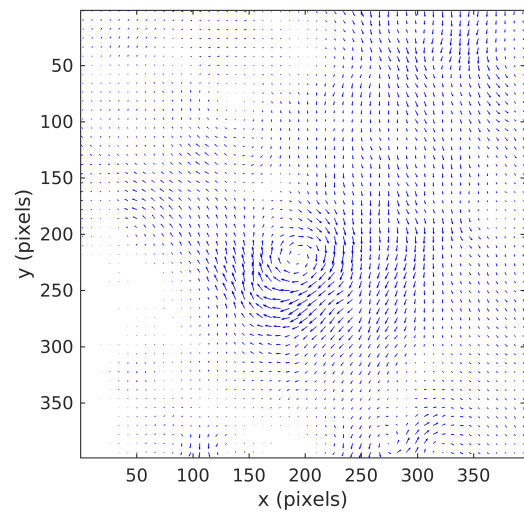


Figure 10: The cloud sequence.

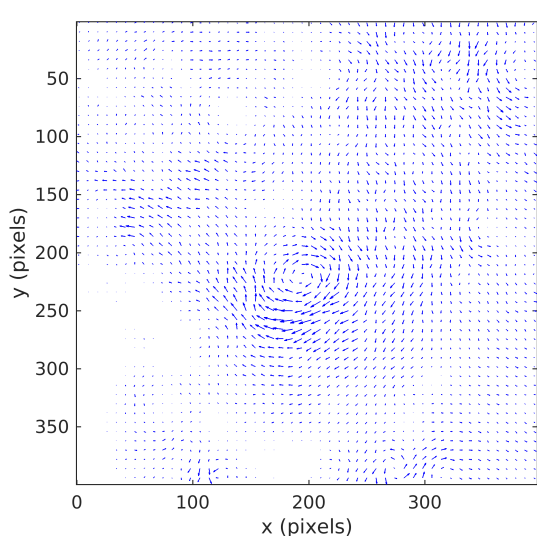


(a) CE with L^2 regularization

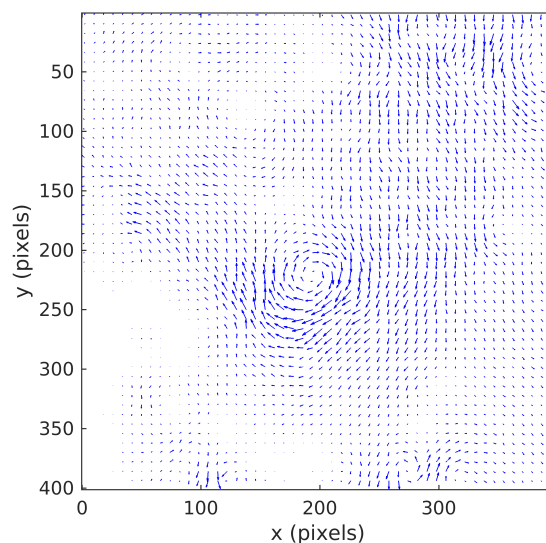


(b) Our refinement with $L^2 - L^2$ approach

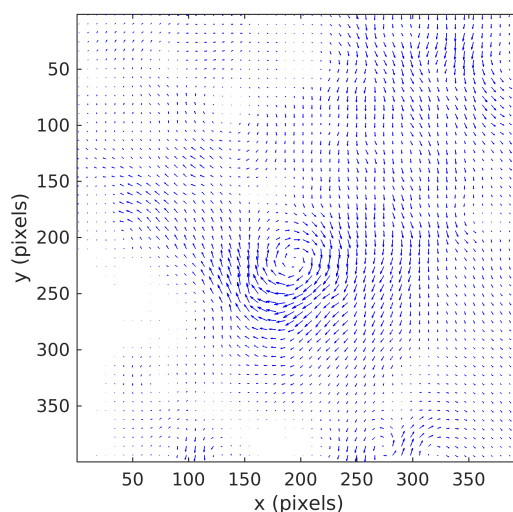
Figure 11: Vorticity plots for the cloud sequence



(a) Our refinement with $L^2 - L^1$ approach



(b) Our refinement with linearized $L^2 - L^1$ approach



(c) Our refinement with median filtering

Figure 12: Vorticity field of the Oseen vortex pairs.

Figure (11a) shows the vorticity plot for the cloud sequence using continuity equation model. As seen from the figure the isotropic behaviour is observed due to the denseness of the flow. Similar denseness is observed in Figures (11b) and (12c) which are obtained using filtering techniques. Figure (12a) shows the refinement with the operator discretization. The isotropic behaviour is not seen in this case. The essential features are only retained. Figure (12b) shows the linearized approximation. The distribution of the x -component of the velocity in Figure (13) further highlights this point.

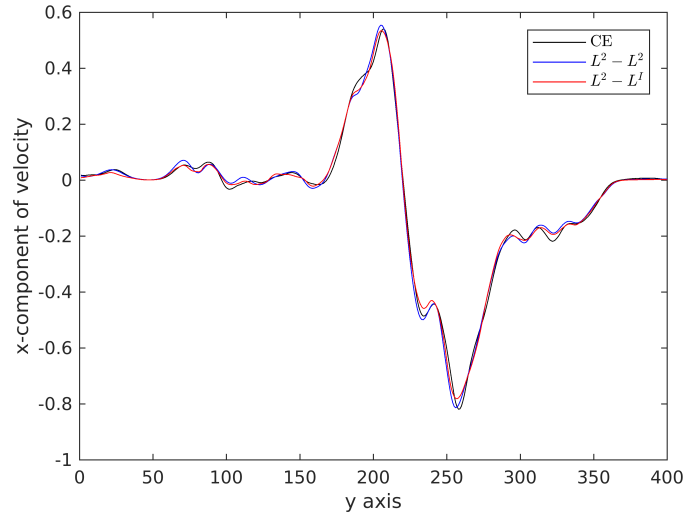


Figure 13: Comparison of the distributions of x -component of the velocity field for the cloud sequence for Figures (11a), (11b) and (12c).

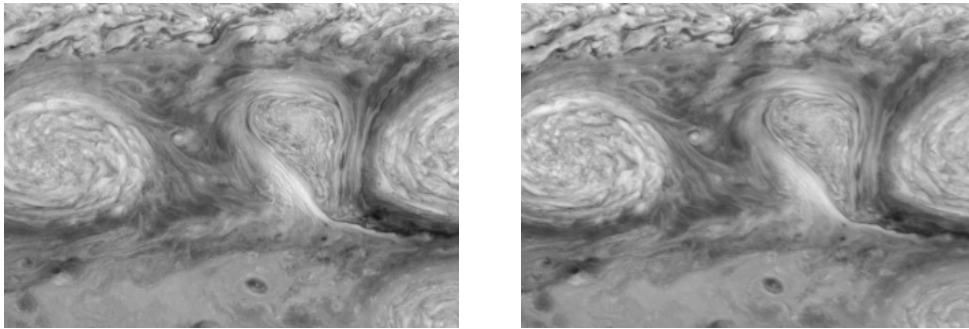


Figure 14: Jupiter's white oval sequence

We now at look at the Jupiter's white oval sequence shown in Figure (14). The oval structures are distinct storms on the surface captured by NASA's Galileo aircraft at a time difference of one hour. Due to this time-lapse there was an observed influence of sun's illumination change on the subsequent image frame. This makes it an interesting motion sequence for optical flow visualization. Here it is necessary to account for this illumination change before applying the optical flow algorithm. For this we use the *correction_illumination* module from [24].

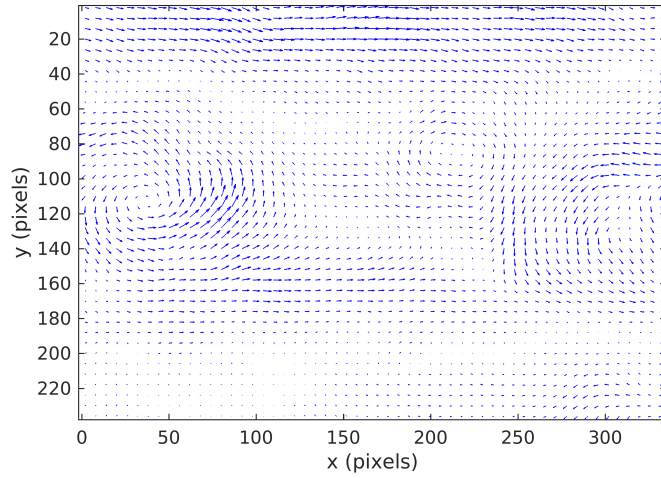
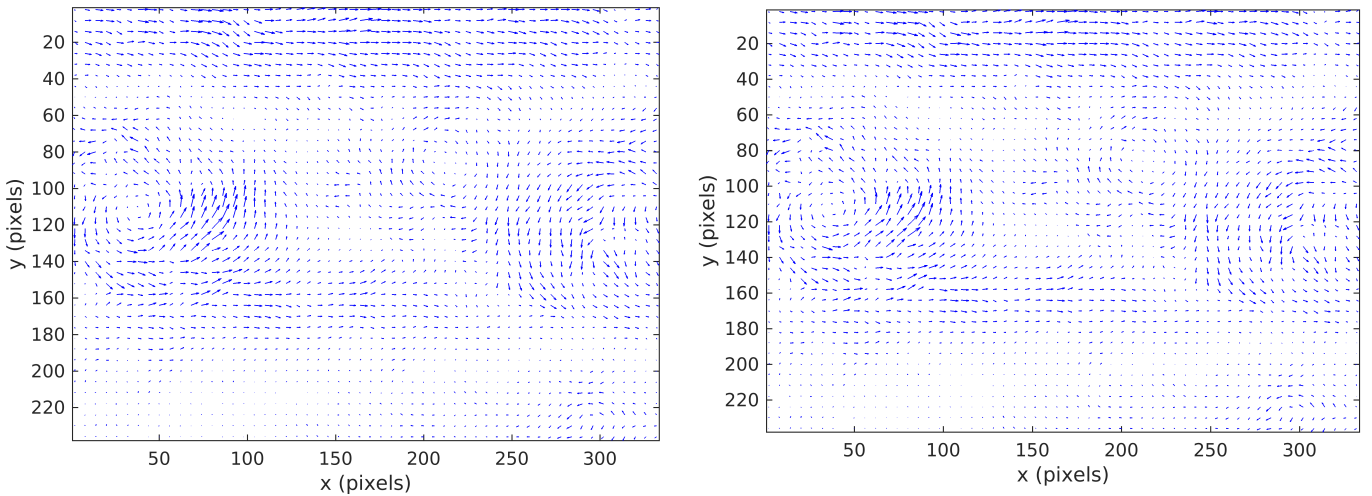


Figure 15: Continuity equation + L^2 regularization with illumination correction.



(a) $L^2 - L^2$ refinement with illumination correction

(b) $L^2 - L^1$ refinement with illumination correction

Figure 16: Vorticity field of the Jupiter's white sequence.

Figures (15) and (16) show the vorticity plots of the Jupiter's white oval sequence using constinuity equation with L^2 regularization and our two approaches with illumination correction respectively. The necessity of illumination correction can be further illustrated with the following comparisons.

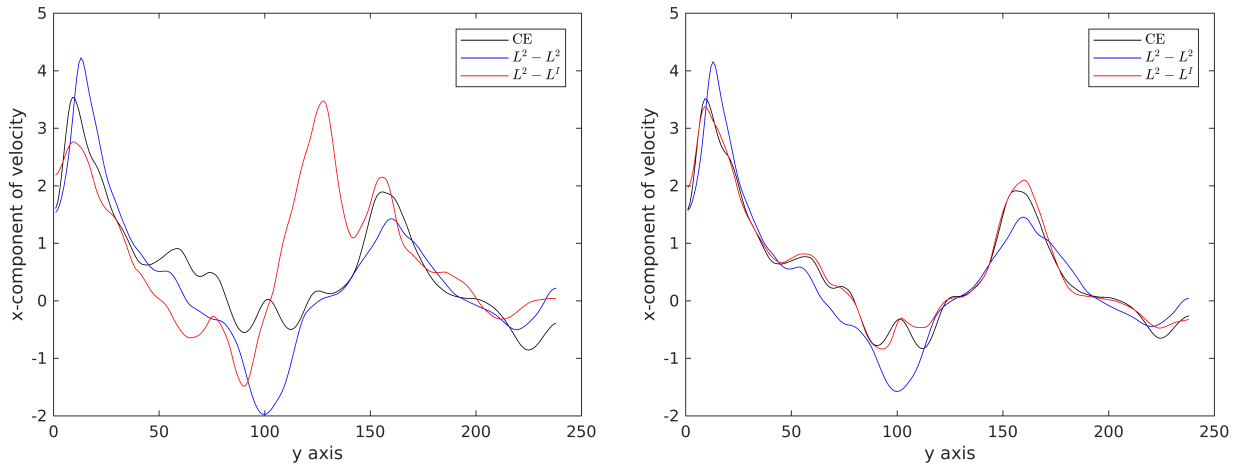


Figure 17: Comparison of the distributions of x -component of the velocity field for the Jupiter's white oval sequence without and with illumination correction.

From the comparison the effect of illumination correction is clearly seen after 30 iterations. There is a large deviation near the two peaks in the first plot when this correction is not performed. In the second plot we see how this difficulty is addressed when the illumination correction is taken into account. We now turn our attention to image sequences which exhibit rigid-body motion. We focus mainly on the sphere image sequence.

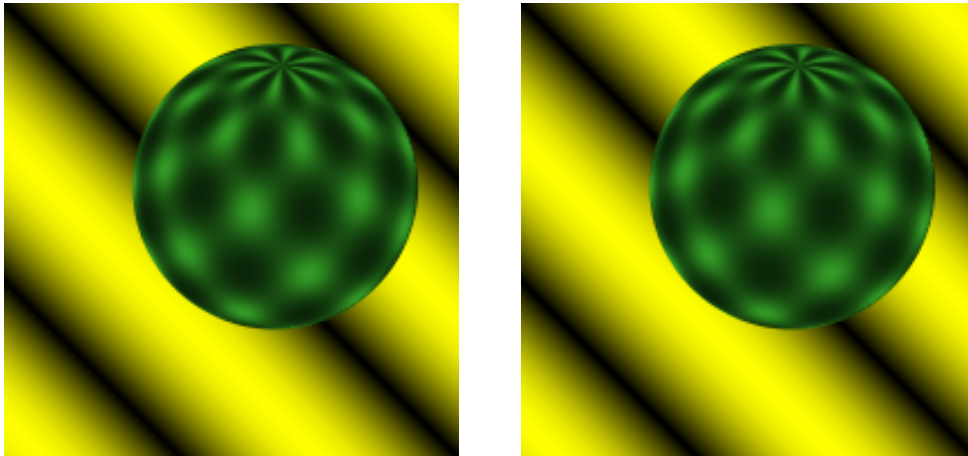


Figure 18: Sphere sequence.

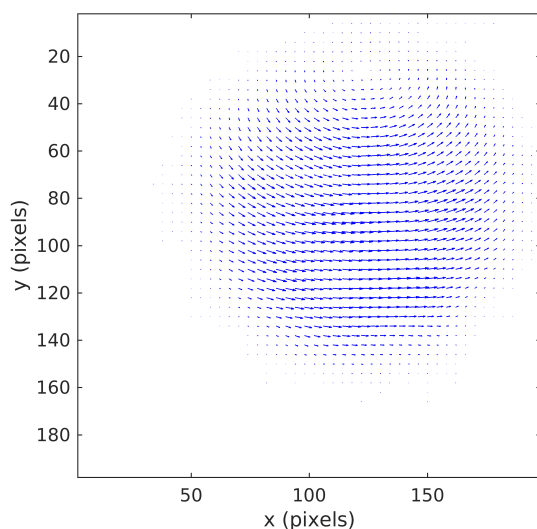
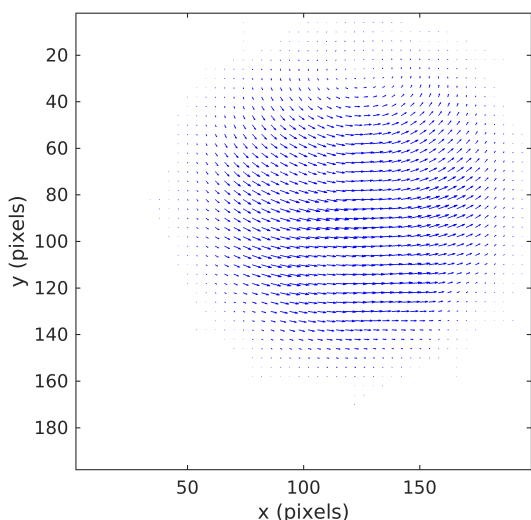
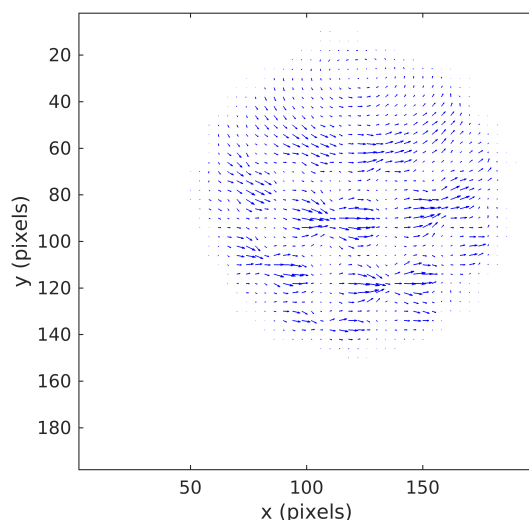


Figure 19: Continuity equation + L^2 regularization on the rotating sphere sequence.



(a) Our refinement with $L^2 - L^2$ approach



(b) Our refinement with $L^2 - L^1$ approach

Figure 20: Transition from fluid to rigid motion estimation.

Figure (20) shows the transition from fluid to rigid motion estimation. In Figure (20a) we can clearly see the isotropic behaviour where no edge informations, textures are captured. To adapt it to rigid body case we changed the α value from 10^2 to 10^6 . This is to ensure more weight is given to the regularization than the additional constraint. Figure (20b) shows the vector field for the $L^2 - L^1$ approach. All the spatial characteristics, discontinuities have been preserved.

3.1 Using Symplectic Gradient

We finally consider two additional constraints $\psi = f^2(\nabla_H \cdot \mathbf{u})^2$ and $\psi = (\nabla_H \cdot \mathbf{u})^2$ where $\nabla_H = (-\partial_y, \partial_x)$ is the orthogonal gradient also known as the symplectic gradient in the literature, see [26]. Unlike the previous constraint which penalizes the divergence of the flow, this penalizes the curl of the flow. Thus these constraints have the ability to capture rotational motions better than the previous constraint. We first show the result for the flow driven case i.e. where $\psi = (\nabla_H \cdot \mathbf{u})^2$.

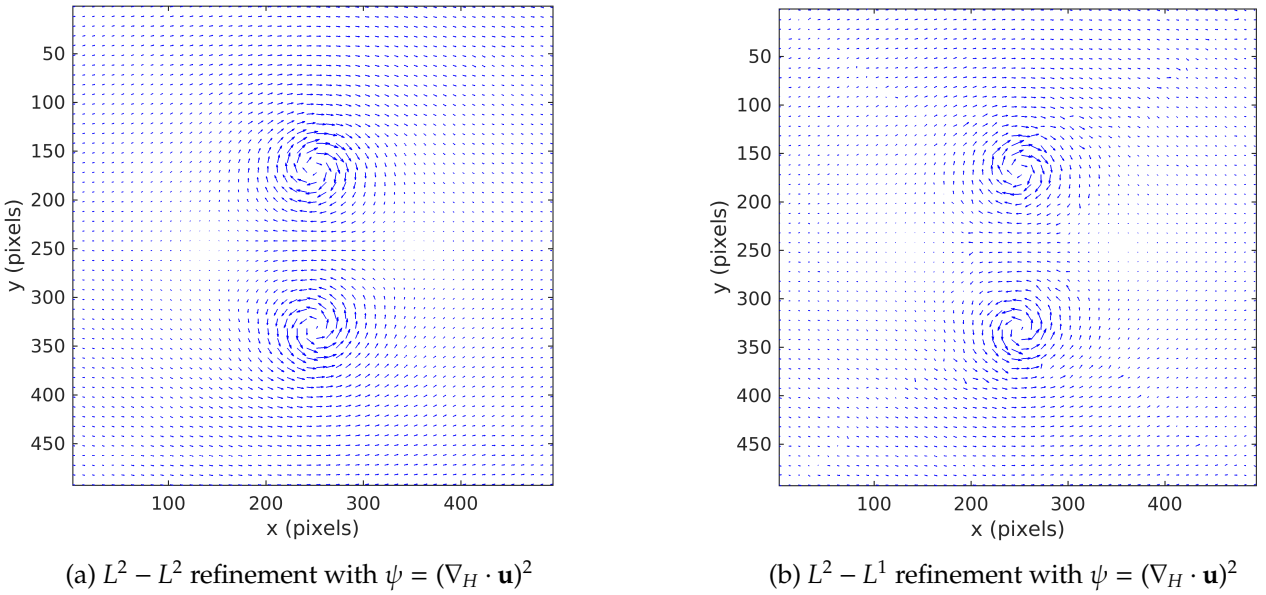


Figure 21: Vorticity plots for the Oseen vortex pair using different constraints.

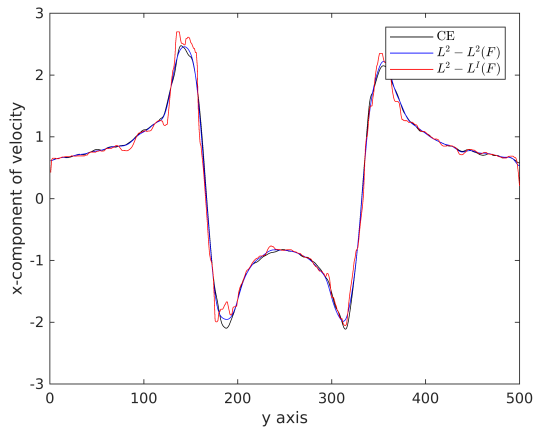
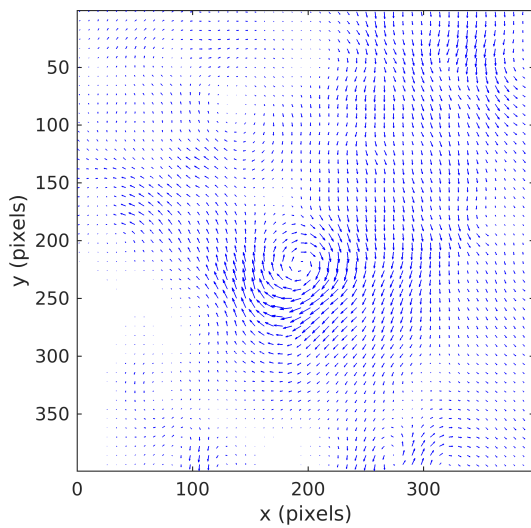
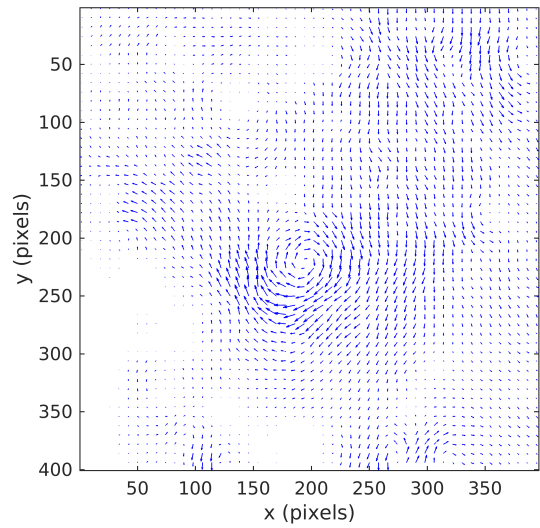


Figure 22: Comparison of the distributions of x -component of the velocity field for the cloud sequence.



(a) $L^2 - L^2$ refinement with $\psi = (\nabla_H \cdot \mathbf{u})^2$



(b) $L^2 - L^1$ refinement with $\psi = (\nabla_H \cdot \mathbf{u})^2$

Figure 23: Vorticity plots for the cloud sequence using different constraints.

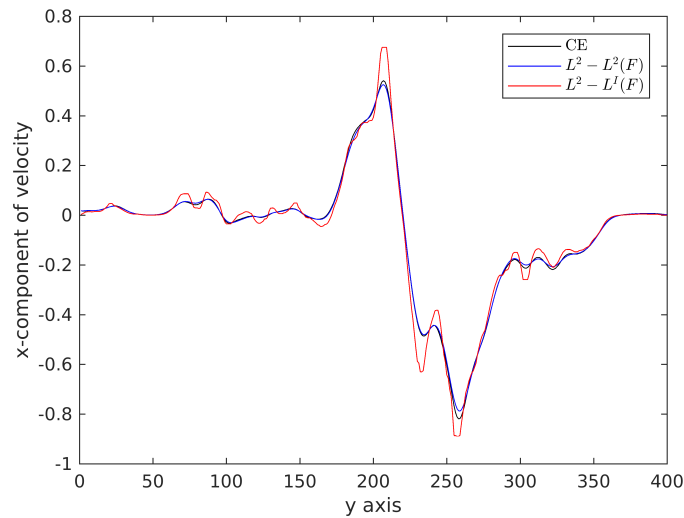


Figure 24: Comparison of the distributions of x -component of the velocity field for the cloud sequence.

The main differences between the two approaches can be seen by running the algorithm for more number of iterations as the following vorticity plots show:

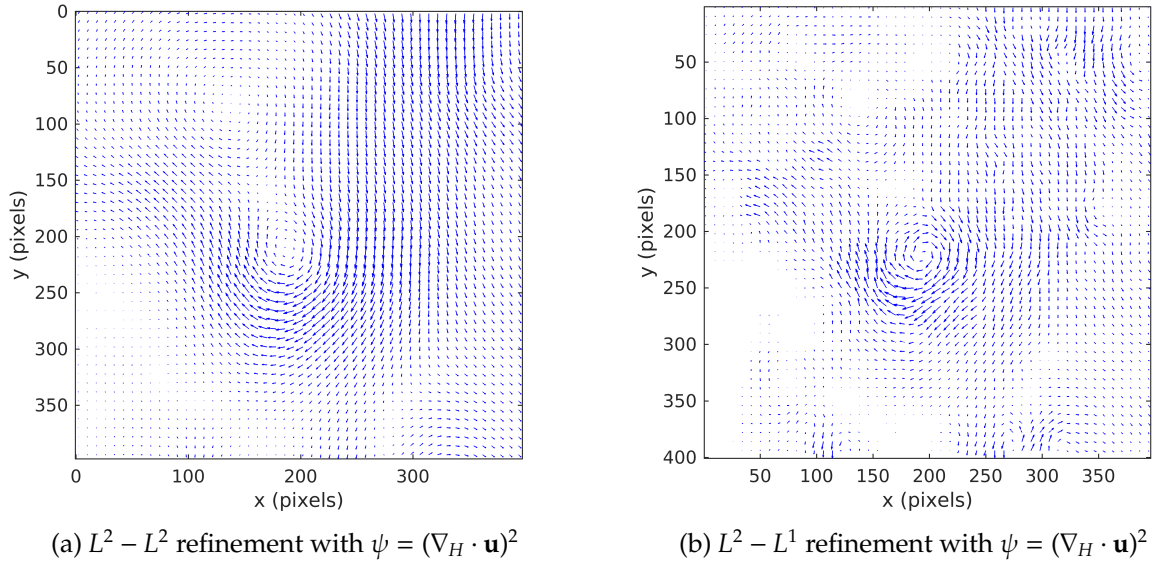


Figure 25: Vorticity field of the cloud sequence after 1000 iterations.

Figure (25a) shows the vorticity plot of our $L^2 - L^2$ refinement algorithm after 1000 iterations. The isotropic diffusive behaviour of the L^2 regularization is seen very clearly in the plot. A similar behaviour is seen for the continuity equation model with L^2 regularization. The same does not hold for the $L^2 - L^1$ approach as the Figure (25b) shows. The level of isotropy is controlled and after a certain number of iterations the rate of diffusion becomes constant. This is mainly due to the L^1 regularization which has preserved only the essential features of the flow.

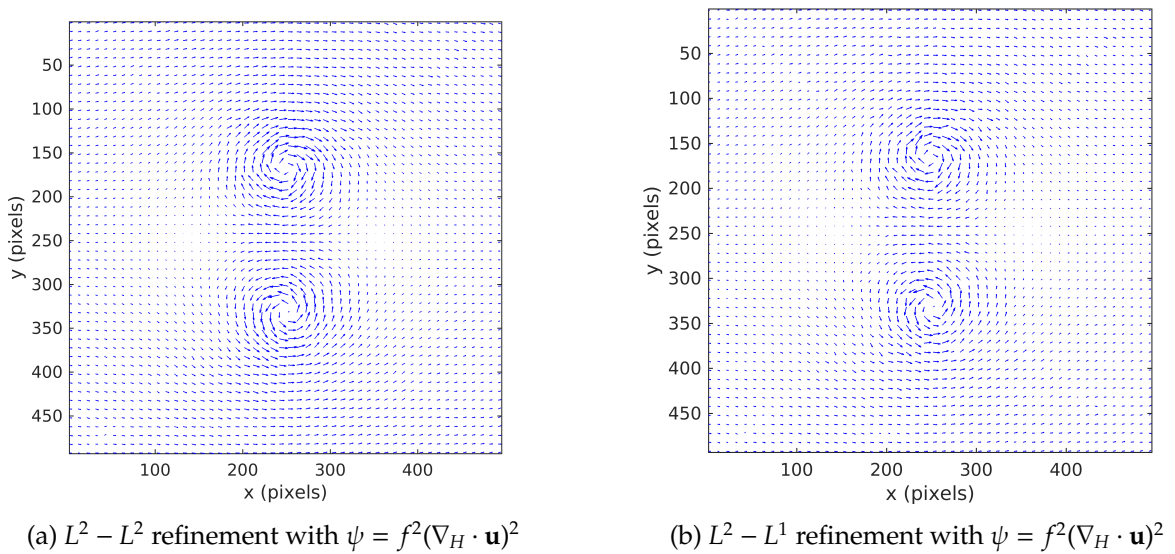


Figure 26: Vorticity field of the Oseen vortex pair.

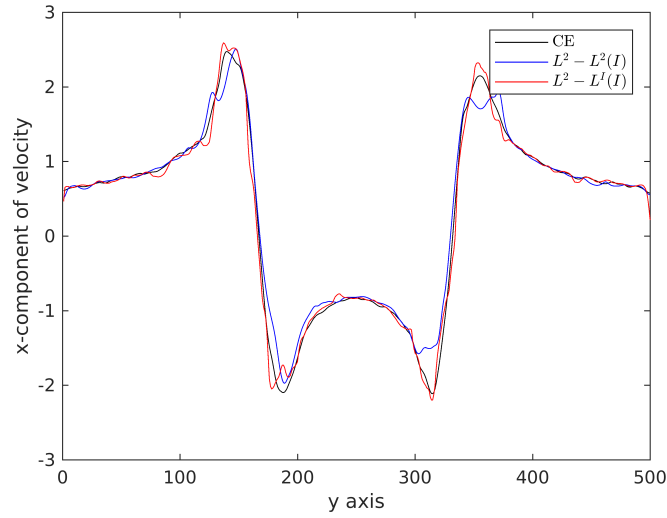
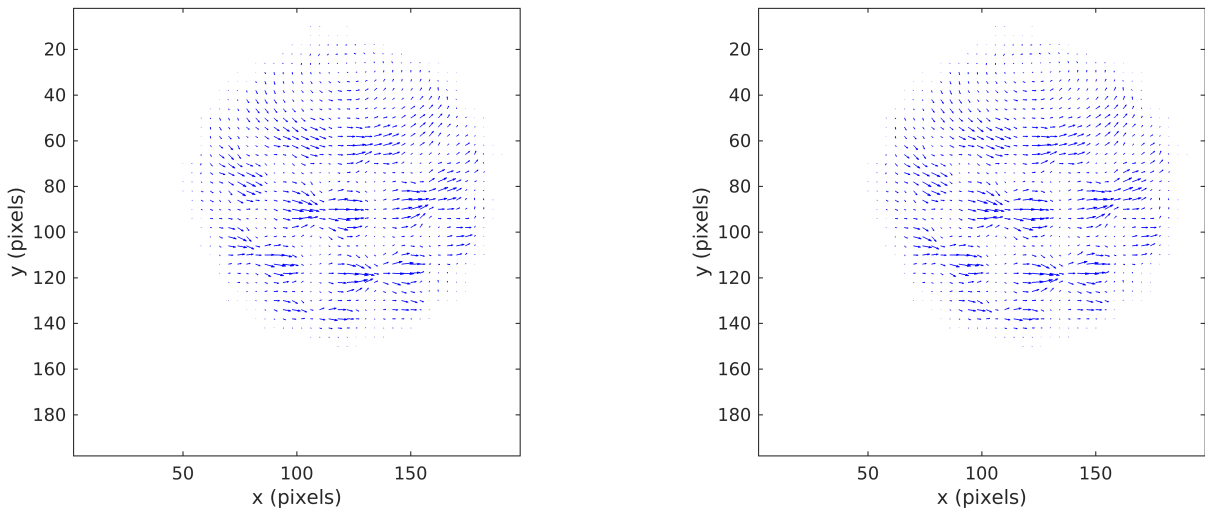


Figure 27: Comparison of the distributions of x -component of the velocity field for the Oseen vortex pair with $\psi = f^2(\nabla_H \cdot \mathbf{u})^2$.



(a) $L^2 - L^1$ refinement with $\psi = f^2(\nabla_H \cdot \mathbf{u})^2$

(b) $L^2 - L^1$ refinement with $\psi = (\nabla_H \cdot \mathbf{u})^2$

Figure 28: Vorticity field of the Oseen vortex pair.

References

- [1] Alvarez L., Esclarin, J., Lefebure M., Sánchez J.: A PDE model for computing optical flow, Proc. XVI Congreso de Ecuaciones Diferenciales y Aplicaciones, 1349-1356 (1999).
- [2] Andreu F., Ballester C., Caselles V. and Mazón J.M.: Minimizing total variation flow. *Differential and Integral Equations*, 14(3), pp.321-360 (2001).

- [3] Aubert G., Deriche R., Kornprobst P.: Computing Optical Flow via Variational Techniques, *SIAM Journal of Applied Mathematics*, Vol. 60, 156-182 (1999).
- [4] Aubert G., Kornprobst P.: *Mathematical Problems in Image Processing, Calculus of Variations and Partial Differential Equations*, Springer, New York (2002).
- [5] Béréziat, D., Herlin, I., Younes, L.: A generalized optical flow constraint and its physical interpretation, *Proceedings of IEEE Conference on Computer Vision and Pattern Recognition* 2, 487-492 (2000).
- [6] Brezis H., *Functional Analysis, Sobolev Spaces and Partial Differential Equations*, Springer, New York (2011).
- [7] Buades A., Chien A., Morel J.M., Osher S.: Topology Preserving Linear Filtering applied to Medical Imaging, *SIAM Journal of Imaging Sciences*, 1(1), 26-50 (2008).
- [8] Burger, M., Dirks H., Frerking L.: On Optical Flow Models for Variational Motion Estimation, *arXiv abs/1512.00298* (2015).
- [9] Cohen I.: Nonlinear variational method for optical flow computation, *Proc. Eight Scandinavian Conf. on Image Analysis*, Vol. 1, 523-530 (1993).
- [10] Chen X., Zillé P., Shao L., Corpetti T.: Optical Flow for Incompressible Turbulence Motion Estimation. *Experiments in Fluids*, Springer Verlag (Germany), (2015).
- [11] Corpetti T., Mémin E., Pérez P.: Estimating Fluid Optical Flow, *Proceedings of the 15th International Conference on Pattern Recognition, ICPR-2000*, Vol. 3, 1033-1036 (2000).
- [12] Corpetti T., Heitz D., Arroyo G., Mémin E., Santa-Cruz A.: Fluid Experimental Flow Estimation based on an Optical Flow Scheme, *Experiments in Fluids*, (2006).
- [13] Corpetti, T., Mémin, E., Pérez, P.: Adaptation of standard optic flow methods to fluid motion. *International Symposium of Flow Visualisation* 1-10, (2000).
- [14] Dacorogna B.: *Direct Methods in Calculus of Variations*, Springer, New York (2008).
- [15] Del Bimbo, A., Nesi, P., Sanz, J. L.: Optical flow computation using extended constraints, *IEEE Transactions on Image Processing*, 5(5), 720-739 (1996).

- [16] Doshi H., Nori Uday Kiran : Constraint-based Refinement of Optical Flow, <https://arxiv.org/abs/2011.12267>.
- [17] Evans L.C.: Partial Differential Equations, Second Edition, American Mathematical Society (2010).
- [18] Hauer D., Mazon J.: Regularizing effects of homogeneous evolution equations: the case of homogeneity of order zero, *Journal of Evolution Equations*, 19, 965-996 (2019).
- [19] Heitz D., Mémin E., Schnörr C.: Variational Fluid Flow measurements from Image Sequences: Synopsis and Perspectives, *Experiments in Fluids*, 48, 369–393 (2010).
- [20] Hinterberger W., Scherzer O., Schnörr C., Weickert J.: Analysis of Optical Flow Models in the Framework of Calculus of Variations, *Numer. Funct. Anal. and Optimiz.*, 23(1&2), 69-89 (2002).
- [21] Horn B.K.P., Schunck B.G.: Determining Optical Flow, *Artificial Intelligence*, Vol. 17, 185-203 (1981).
- [22] Kumar A., Tannenbaum A., Balas G., Optical flow: A curve evolution approach, *IEEE Transactions of Image Processing* 5, 598-611 (1996).
- [23] Le Dret H., Lucquin B.: Partial Differential Equations: Modeling, Analysis and Numerical Approximation, Birkhäuser, Springer (2016).
- [24] Liu T.: OpenOpticalFlow: An Open Source Program for Extraction of Velocity Fields from Flow Visualization Images, *Journal of Open Research Software*, 5:29 (2017).
- [25] Liu T., Shen L.: Fluid Flow and Optical Flow, *Journal of Fluid Mechanics*, 614, 253-291 (2008).
- [26] Luttmann A., Bollt E.M., Basnayake R., Kramer S., Tufillaro N.B.: A Framework for Estimating Potential Fluid Flow from Digital Imagery, *Chaos: An Interdisciplinary Journal of Nonlinear Science*, Vol. 23, 3 (2013).
- [27] Martin A., Schiavi E., de Léon S.S.: On 1-Laplacian elliptic equations modeling magnetic resonance imaging Rician denoising, *Journal of Mathematical Imaging and Vision*, 57:202-224 (2017).
- [28] Mazon J., The Total Variation Flow, Lecture Notes.
- [29] Nagel H.H.: On the estimation of optical flow: relations between different approaches and some new results, *Artificial Intelligence* 33, 299-324 (1987).

- [30] Sapiro G.: Geometric Partial Differential Equations and Image Analysis, Cambridge University Press, New York (2001).
- [31] Oberman A.M.: A Convergent Monotone Difference Scheme for Motion of Level Sets by Mean Curvature, *Numer. Math.* 99, 365-379 (2004).
- [32] Scherzer O., Grasmair M., Grossauer H., Haltmeier M., Lenzen F.: Variational Methods in Imaging, Springer, New York (2009).
- [33] Schunck B.G.: The motion constraint equation for the optical flow, *Proceedings of the International Conference of Pattern Recognition*, 20-22 (1984).
- [34] Schunck B.G.: Image flow continuity equations for motion and density, *Proceedings of Workshop Motion: Representation and Analysis*, 89-94 (1986).
- [35] Schnörr C.: Determining optical flow for irregular domains by minimizing quadratic functionals of a certain class, *International Journal of Computer Vision*, Vol. 6, 25-38 (1991).
- [36] Wang B., Cai Z., Shen L., Liu T.: An Analysis of Physics-based Optical Flow, *Journal of Computational and Applied Mathematics*, 276, 62-80 (2015).
- [37] Wei L., Agarwal R. P., Wong P.J.Y.: Existence and iterative construction of solutions to non-linear Dirichlet boundary value problems with p -Laplacian operator, *Complex Variables and Elliptic Equations: An International Journal*, 55:5-6, 601-608 (2010).
- [38] Weickert J., Schnörr C.: A Theoretical Framework for Convex Regularizers in PDE-based Computation of Image Motion, *International Journal of Computer Vision*, 45, 245-264 (2001).
- [39] Wildes R.P., Amabile M.J., Lanzillotto A., Leu T.: Recovering Estimates of Fluid Flow from Image Sequence Data, *Computer Vision and Image Understanding*, 80, 246-266 (2000).